AIAA/AAS Astrodynamics Specialist Conference
13 - 16 August 2012, Minneapolis, Minnesota

AIAA 2012-4666

Regions Near the Libration Points Suitable to Maintain Multiple Spacecraft

A. Héritier* and K. C. Howell†

Purdue University, West Lafayette, Indiana, 47906, USA

Regions near the libration points that might prove suitable to maintain multiple spacecraft in formation are explored. For a small distance between the spacecraft, these regions represent quadric surfaces and are derived analytically. For larger formations, quasi-periodic Lissajous trajectories are employed as a tool to determine regions that maintain spacecraft placed at large mutual distances. These low drift regions are examined during the star observation phase using a large telescope-occulter formation and compared to the analytical approximations. Placing the occulter in these regions results in a reduction in the control effort to maintain both the mutual distance between the spacecraft and the specified formation pointing direction.

I. Introduction

Within the last decade, hundreds of planets orbiting other stars, called extrasolar planets or exoplanets, have been detected. Thus far, most of them are gas giants like Jupiter, but improvements in technology are moving the detection limits to planets with smaller masses. Some new concepts using large formations can detect not only Earth-like planets, but can also characterize them via spectroscopy, providing information such as atmospheric conditions, internal structure, mass estimates, as well as life signs. For example, the original New Worlds Observer (NWO) design concept employs an external occulter placed at a relatively large distance (∼80,000 km) from its telescope for the detection and characterization of extrasolar planets.[1] In the science mode, the occulter is maintained along the line-of-sight from the telescope to the target star to block out the starlight. It suppresses the starlight by many orders of magnitude, to enable the observation of habitable terrestrial planets. From a control perspective, the telescope-occulter architecture concept can be decomposed into two mission phases.

- The observation phase: the occulter must be maintained precisely along the telescope line-of-sight to some inertially fixed target stars.
- The reconfiguration phase: the occulter is realigned between each observation from one target star line-of-sight to the next.

During the observation mode, the two spacecraft must be aligned within a few meters along the star line-of-sight. This is most easily accomplished if these spacecraft are in a low-acceleration environment such as the vicinity of the L_2 Sun-Earth libration point. The L_2 Sun-Earth libration point region provides a relatively cold environment, far away from the disturbances of the Sun and therefore ideal for astronomical instruments. This region has been a popular destination for satellite imaging formations. Barden and Howell investigate the natural behavior on the center manifold near the L_2 Sun-Earth libration point and compute some natural six-spacecraft formations, which demonstrate that quasi-periodic trajectories could be useful for formation flying.[2] Later, Marchand and Howell extend this study and use some control strategies, continuous and discrete, to maintain non-natural formations near the libration points.[3] Formation flying missions and many current proposals typically examine spacecraft separated by small distances. Within

*Ph.D., School of Aeronautics and Astronautics, Purdue University, West Lafayette, Indiana, 47907; Currently Advanced Concepts Team, ESTEC, PPC-PF, Keplerlaan 1 - 2201 AZ Noordwijk - The Netherlands; Email: Aurelie.Heritier@esa.int.

†Hsu Lo Professor of Aeronautical and Astronautical Engineering, School of Aeronautics and Astronautics, Purdue University, West Lafayette, Indiana, 47907; Email: howell@purdue.edu.

that context, space-based observatory and interferometry missions, such as the Terrestrial Planet Finder, have been the motivation for the analysis of many control strategies. Gómez et al. investigate discrete control methods to maintain the relatively small formation.[4] Howell and Marchand consider linear optimal control, as applied to nonlinear time-varying systems, as well as nonlinear control techniques, including input and output feedback linearization.[5] Hsiao and Scheeres implement position and velocity feedback control laws to force a formation of spacecraft to possess a rotational motion relative to a nominal trajectory.[6,7] Recently, Gómez et al. derive regions around a halo orbit with zero relative velocity and zero relative radial acceleration that ideally maintain the mutual distances between spacecraft.[8] The analysis by Gómez et al., based on linearization relative to the reference orbit, assumes small formations of spacecraft.

New mission concepts regarding spacecraft placed at larger relative distances have increased the interest in large formations. Lo examines the Terrestrial Planet Finder architecture with an external occulter at a much larger relative distance, and considers different mission scenarios with the formation placed on a halo orbit around the Sun-Earth L_2 libration point as well as a formation on a Earth leading heliocentric orbit.[9] Millard and Howell evaluate some control strategies for the Terrestrial Planet Finder-Occulter mission for the two phases of the mission concept, that is, observation and reconfiguration phases.[10] They compare different control methods for satellite imaging arrays in multi-body systems such as optimal nonlinear control, geometric control methods, a linear quadratic regulator and input state feedback linearization. Kolemen and Kasdin focus on the realignment problem and investigate optimal control strategies for the reconfiguration phase, to enable the imaging of the largest possible number of planetary systems with the minimum mass requirement.[11] The analysis by Kolemen and Kasdin does not exploit the natural dynamics specific to the region near the libration points. Most recently, Héritier and Howell then investigate the natural dynamics in the collinear libration point region for the control of large formations.[12] They derive natural regions that maintain large formations for space observations. This current analysis details and expands on the initial work of Héritier and Howell. A more general understanding of these natural regions suitable for formation flight is examined for formations of spacecraft of any size along various reference trajectories. Analytical expressions of these natural regions are also derived to explain their shape and orientation in space.

This investigation explores the dynamical environment near the L_2 Sun-Earth libration point to aid in the control of a formation of spacecraft of any size, in terms of the relative distance between vehicles. By exploiting the natural dynamics within the Circular Restricted Three-Body Problem (CR3BP), natural regions suitable to maintain small and large formations are determined. Regions along a specified reference path that represent suitable locations to maintain small formations are first examined. These suitable zones are derived analytically using variational equations relative to the reference path. These regions represent quadric surfaces of two types, either ellipsoids or elliptic cylinders, and the relationship between the type of quadric surfaces and the eigenstructure of the reference trajectory is investigated. Then, the behavior at much larger distances from a specified reference trajectory, due solely to the natural dynamics, is explored for the placement of large formations of spacecraft. Quasi-periodic Lissajous trajectories are employed as a tool to determine regions that maintain spacecraft placed at large mutual distances. Extensive computations of quasi-periodic Lissajous trajectories near a given reference orbit are completed. Arcs along the Lissajous trajectories are analyzed and viewing spheres at various points along the reference orbit are developed. These space spheres are used as a tool to categorize regions along the orbit with less natural drift when the distance between two vehicles is large. Locating a large formation in these zones leads to a smaller variation in the mutual distance between the spacecraft and the pointing direction of the formation. Finally, the low natural drift regions are employed for the observation of inertially-fixed target stars using a large telescope-occulter formation. The occulter is maintained via a linear quadratic regulator during the observation phase. Observing the target stars when the formation lies in a low natural drift zone reduces the control effort to maintain the telescope-occulter formation, particularly for longer observation intervals.

II. Dynamical Model

The motion of the spacecraft is described within the context of the CR3BP. In this model, it is assumed that the Sun and the Earth move in a circular orbit around their barycenter. The mass of the spacecraft is negligible compared to the masses of the two primaries. The equations of motion are described in a rotating coordinate frame where the spacecraft is located relative to the barycenter of the primaries, with the $\hat{x}$-axis in the rotating frame directed from the Sun to the Earth. Let $\bar{X}$ define a general vector in the rotating frame

describing the motion of the spacecraft, i.e.

$$\bar{X}(t) = [x \quad y \quad z \quad \dot{x} \quad \dot{y} \quad \dot{z}]^T \tag{1}$$

where superscript 'T' implies transpose. The equations of motion are expressed in terms of a pseudo potential function

$$U = \frac{(1-\mu)}{r_1} + \frac{\mu}{r_2} + \frac{1}{2}(x^2 + y^2) \tag{2}$$

with $r_1 = \sqrt{(x+\mu)^2 + y^2 + z^2}$ and $r_2 = \sqrt{(x-(1-\mu))^2 + y^2 + z^2}$, and where μ is the mass parameter associated with the Sun-Earth system. The scalar nonlinear equations of motion in their non-dimensional forms are then written as

$$\ddot{x} - 2\dot{y} = U_x \tag{3}$$

$$\ddot{y} + 2\dot{x} = U_y \tag{4}$$

$$\ddot{z} = U_z \tag{5}$$

where U_j represents the partials $\frac{\partial U}{\partial j}$ for $j = x, y, z$. The design process generally relies on variations relative to a reference trajectory. Given a solution to the nonlinear differential equations, linear variational equations of motion are derived in matrix form as

$$\delta\dot{\bar{X}}(t) = A(t)\delta\bar{X}(t) \tag{6}$$

where $\delta\bar{X}(t) = \bar{X}(t) - \bar{X}_{ref}(t) = [\delta x \quad \delta y \quad \delta z \quad \delta\dot{x} \quad \delta\dot{y} \quad \delta\dot{z}]^T$ represents variations about a reference trajectory. The $A(t)$ matrix is time-varying of the form

$$A(t) = \begin{bmatrix} 0_{3\times3} & I_{3\times3} \\ F & J \end{bmatrix} \tag{7}$$

where the F matrix and J matrix are defined as

$$F = \begin{bmatrix} U_{xx} & U_{xy} & U_{xz} \\ U_{yx} & U_{yy} & U_{yz} \\ U_{zx} & U_{zy} & U_{zz} \end{bmatrix} \tag{8}$$

$$J = \begin{bmatrix} 0 & 2 & 0 \\ -2 & 0 & 0 \\ 0 & 0 & 0 \end{bmatrix} \tag{9}$$

The symbol U_{jk} represents the partials $\frac{\partial U^2}{\partial j \partial k}$ for $j, k = x, y, z$ and these partials are evaluated along the reference path. The general form of the solution to Eq. (6) is

$$\delta\bar{X}(t) = \Phi(t, t_0)\delta\bar{X}(t_0) \tag{10}$$

where $\Phi(t, t_0)$ is the state transition matrix (STM), which is essentially a linear mapping that approximates the impact of the initial variations on the variations downstream. The STM satisfies the matrix differential equation

$$\dot{\Phi}(t, t_0) = A(t)\Phi(t, t_0) \tag{11}$$

$$\Phi(t_0, t_0) = I_{6\times6} \tag{12}$$

where $I_{6\times6}$ is the identity matrix. Eq. (11) is integrated simultaneously with the nonlinear equations of motion to generate reference states and updates to the trajectory. Since the STM is a 6 x 6 matrix, it requires the integration of 36 first-order, scalar, differential equations, plus the additional 6 first-order state equations, hence a total of 42 differential equations.

One advantage of the CR3BP as the framework for this analysis lies in its dynamical properties that may be exploited for mission design. The equations of motion in the CR3BP possess five equilibrium solutions, or libration points. These consist of the three collinear points (L_1, L_2, and L_3) and the two equilateral

points (L_4 and L_5). In the vicinity of each equilibrium point, some structure can be identified: periodic and quasi-periodic orbits (center manifold), as well as unstable and stable manifolds. Knowledge of this natural flow is very useful for trajectory design. One well-known type of periodic trajectory is the set of halo orbit families that are symmetric across the $(\hat{x}, \hat{z})$ rotating plane. These orbits are of particular interest and frequently serve as baseline trajectories for mission design. The northern halo orbit family near the L_2 Sun-Earth libration point appears in Figure 1. Two halo orbits with different amplitudes are selected in this

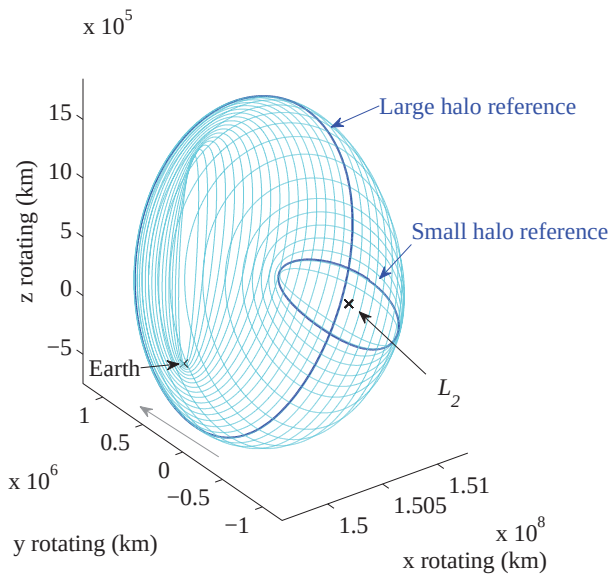

Figure 1. Northern halo family near the L_2 Sun-Earth libration point

family as reference trajectories for this investigation. The reference orbits appear in dark blue in Figure 1. They are denoted as either 'small' or 'large' reference orbits throughout this analysis to distinguish them. The approximative amplitudes A_y and A_z along the $\hat{y}$ and $\hat{z}$ axes, respectively, are listed in Table 1.

Table 1. Amplitudes A_y and A_z of the two selected reference orbits

Reference orbits	Amplitude $A_y(km)$	Amplitude $A_z(km)$
Small halo reference	680,000	150,000
Large halo reference	1,000,000	2,000,000

III. Natural Regions Suitable for Small Formations

The first objective in this investigation is a better understanding of the dynamical environment at small distances from a specified reference path. A chief spacecraft evolves along the given reference trajectory represented in Figure 1. To describe the position of a deputy vehicle relative to the chief spacecraft, spheres of points at each time along the reference orbit are defined as illustrated in Figure 2. The spheres are enlarged in the figure for illustration, and their actual radius reflects a specified baseline distance that is assumed between the vehicles. At each time along the reference, the chief spacecraft is positioned at the center of a sphere. A deputy vehicle is then located somewhere on the surface of the sphere. A vector defined from the chief spacecraft to the deputy vehicle defines a direction or orientation for the formation. Every direction on the sphere is investigated at each time along the reference orbit and some specific directions on the spheres are derived that represent suitable locations to maintain small formations.

III.A. Low Drift Regions Derived via Variational Equations

Natural regions close to the given chief reference path are derived to maintain small formations of spacecraft. Ideally, regions with zero relative velocity and zero relative acceleration maintain the mutual distance between the spacecraft and the pointing direction orienting the formation.[13] Assuming that the separation between

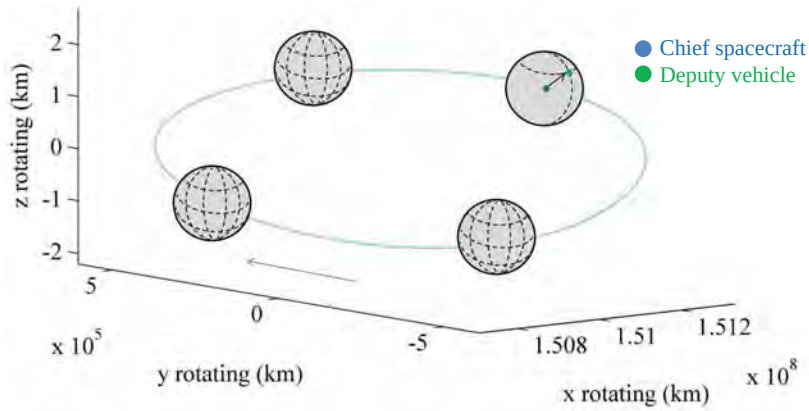

Figure 2. Spheres of test points relative to the chief spacecraft along the chief reference trajectory (enlarged size for illustration)

the spacecraft is small, no greater than a few kilometers at most, the regions of low drift are derived via the first-order variational equations defined in Equation (6), with respect to the given reference orbit. These variational equations are rewritten in terms of three-dimensional relative position and relative velocity vectors as

$$\begin{bmatrix} \delta\dot{\bar{r}} \\ \delta\ddot{\bar{r}} \end{bmatrix} = \begin{bmatrix} 0_{3\times3} & I_{3\times3} \\ F & J \end{bmatrix} \begin{bmatrix} \delta\bar{r} \\ \delta\dot{\bar{r}} \end{bmatrix} \tag{13}$$

where $\delta\bar{r} = [\delta x \quad \delta y \quad \delta z]^T$ and $\delta\dot{\bar{r}} = [\delta\dot{x} \quad \delta\dot{y} \quad \delta\dot{z}]^T$. The F matrix and J matrix are defined in Equation (8) and Equation (9), respectively. For the spacecraft placed at a small distance with respect to each other, the relative velocity in an ideal direction is assumed to be zero, i.e., $\delta\dot{\bar{r}} = \bar{0}$. Notice that this assumption is only valid for a small formation of spacecraft. At larger distances, the relative velocity may not be negligible. Under this assumption, however, from Equation (13), the relative acceleration is then

$$\delta\ddot{\bar{r}} = F\delta\bar{r} \tag{14}$$

The goal in this investigation is the identification of some natural regions, on the sphere, that is, natural directions or orientations, that not only maintain the mutual distance between the spacecraft but also the orientation of the formation. Assuming no relative velocity between the spacecraft, regions that also possess zero relative acceleration would ideally maintain the formation. The norm of the relative acceleration is computed from the dot product of $\delta\ddot{\bar{r}}$ with $\delta\ddot{\bar{r}}$, i.e.,

$$\|\delta\ddot{\bar{r}}\|^2 = \delta\ddot{\bar{r}} \cdot \delta\ddot{\bar{r}} = F\delta\bar{r} \cdot F\delta\bar{r} \tag{15}$$

The locations such that the relative acceleration is equal to zero are then the set of points that satisfy the equation

$$\delta\bar{r}^T F^T F\delta\bar{r} = 0 \tag{16}$$

The analytical expression defined in Equation (16) represents regions with zero relative velocity and zero relative acceleration. Placing spacecraft in these low drift regions avoids large variations in their mutual distances while maintaining the orientation of the formation.

To numerically compute the low drift regions, a location along the reference trajectory is first selected that represents the state of the chief spacecraft. Relative to this location, a sphere of points that corresponds to a radius equal to 1 km is defined. Such a sphere of points is illustrated in Figure 3. The center of the sphere represents the selected location on the reference arc, i.e., the location of the chief spacecraft. The test points are then parametrized by two angles, an in-plane angle θ measured from the $\hat{x}$-axis in the rotating frame and an out-of-plane angle β defined relative to the $(\hat{x}, \hat{y})$-plane. The velocity of all the points on the sphere is assumed to be equal to the velocity of the selected location on the reference trajectory in this linear analysis since $\delta\dot{\bar{r}}$ is assumed as zero. The relative acceleration that corresponds to each of the states on the sphere is evaluated using the right side of Equation (15), and the states on the sphere that possess

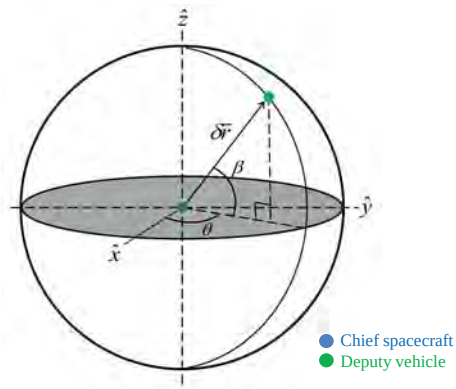

Figure 3. Sphere of test points described by in-plane angle θ and out-of-plane angle β

the smallest values for the relative acceleration represent the low drift regions. For a fixed distance between the spacecraft, these low drift regions are represented by a collection of points on the sphere; they generally result a ring shape. Such rings are illustrated in Figure 4(a) at different times along the reference trajectory. The reference path in the figure corresponds to the small halo reference orbit previously defined in Figure 1. One ring-shaped surface at the location that is identified at time $t = 100$ days from the initial location along the reference path is represented in Figure 4(b). The distance between the two spacecraft is selected as 1 km for the simulation, i.e., the radius of the rings is equal to 1 km, but the size of the rings is enlarged in the figure for illustration. If the chief spacecraft evolves along this reference orbit, placing a deputy spacecraft on the surface of the rings maintains the formation relatively well, i.e, both the distance between the spacecraft and the pointing direction that orients the formation remains fairly constant.

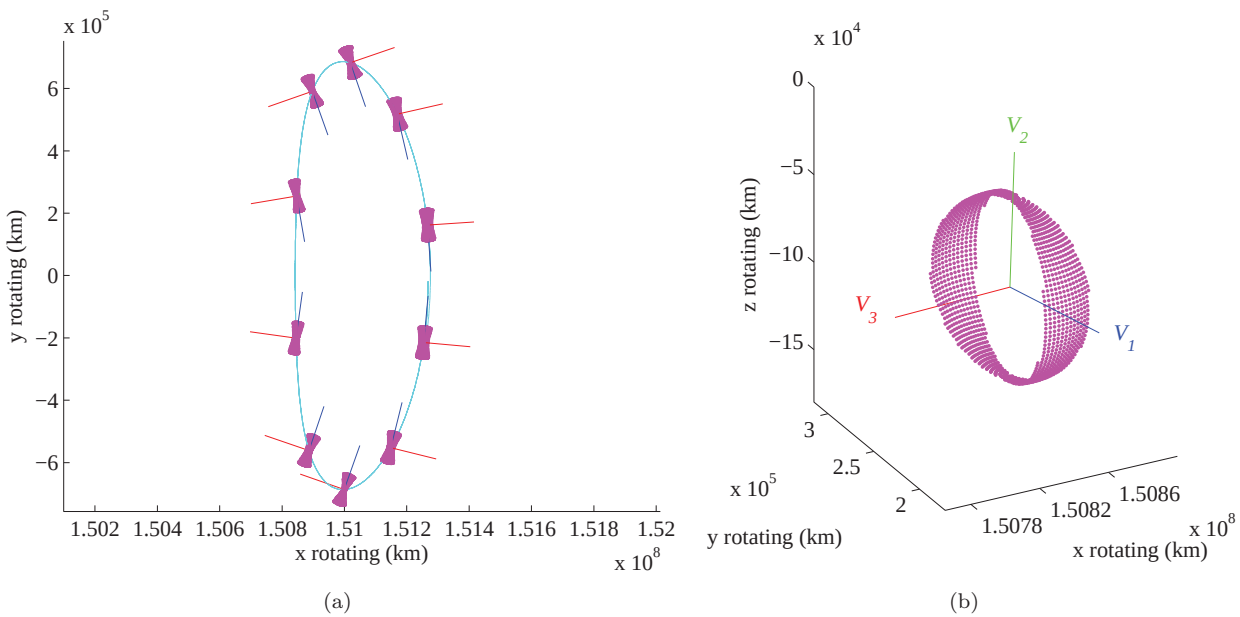

Figure 4. (a) Ring-shaped surfaces with zero relative velocity and zero relative acceleration along the small halo reference orbit; (b) One ring-shaped surface at time $t = 100$ days along the small halo reference orbit (enlarged in size for illustration)

III.B. Surfaces of Relative Accelerations

The relative acceleration between a deputy vehicle and its chief spacecraft has its lowest values in the low drift regions on the spheres but it never precisely reaches zero. The values for the relative acceleration between the spacecraft are derived at one location along the reference trajectory, to illustrate how the relative acceleration

varies with respect to the relative directions on the sphere. The relative acceleration and its characteristics on the surface of the sphere are similar for all locations along this small halo reference orbit. One specific location, identified as time $t = 118$ days along the reference path, is selected and represents the state for the chief spacecraft. A set of test points on a sphere of radius 1 km is defined around this location, and the norm square of the relative acceleration for each of these points is evaluated using the right side of Equation (15). The norm square of the relative acceleration is then plotted as a function of the two angles θ and β defined previously in Figure 3. The surface of relative acceleration at time $t = 118$ days along the small halo reference orbit is represented in Figure 5(a), and a 2D projection of the surface plot appears in Figure 5(b) associated with $\beta = 0$ degrees. The corresponding sphere of points at time $t = 118$ days along the reference orbit is

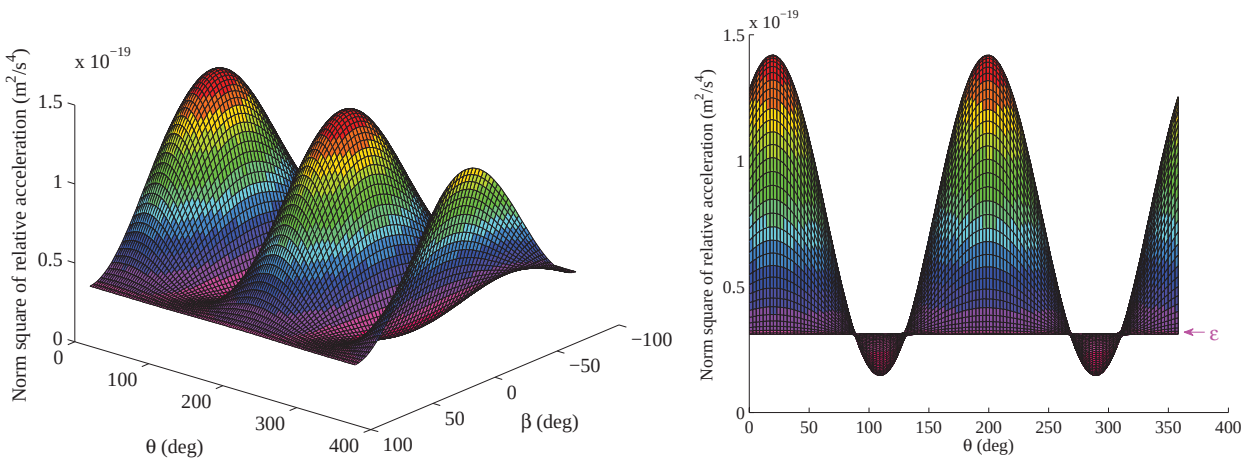

(a) (b)

Figure 5. Surface of the norm square of the relative acceleration at the location that is identified as $t = 118$ days from the initial location along the small reference orbit; (a) 3D view; (b) 2D view at $\beta = 0$ degrees

illustrated in Figure 6. The colors on the sphere reflect the value of the relative acceleration at the specific locations on the sphere. The locations colored in pink correspond to the low drift region of the sphere, that

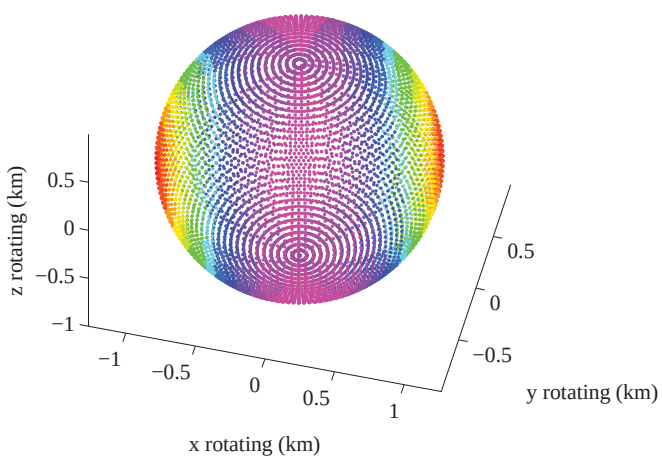

Figure 6. Sphere of test points colored by relative acceleration at the chief location that is identified as $t = 118$ days from the initial location along the small reference orbit

is where the relative acceleration has the smallest values. As the relative acceleration between the spacecraft never precisely reaches zero, a small positive coefficient, denoted ϵ, is introduced for the computation of the low drift regions. Equation (16) is then rewritten as

$$\delta\bar{r}^T F^T F \delta\bar{r} \leq \epsilon \tag{17}$$

The ϵ coefficient corresponds to the desired maximum value for the relative acceleration in the low drift region. Depending on the value for ϵ, the low drift region can cover a smaller or larger portion of the sphere.

In this investigation, the value for ϵ is selected such that the low drift regions cover a ring-shaped surface on the spheres. This value is represented in Figure 5(b).

III.C. Low Drift Regions as Quadric Surfaces

By considering the analytical expression for the low drift zones derived in Equation (17), it is apparent that these low drift regions are represented as quadric surfaces. Using a change in coordinate, Equation (17) is transformed into its canonical form. The F matrix is a real symmetric matrix, i.e., $F = F^T$ and, therefore, can be diagonalized. The singular value decomposition of F then takes the form

$$F = P\Delta P^T = \begin{bmatrix} \bar{V}_1 & \bar{V}_2 & \bar{V}_3 \end{bmatrix} \begin{bmatrix} \lambda_1 & 0 & 0 \\ 0 & \lambda_2 & 0 \\ 0 & 0 & \lambda_3 \end{bmatrix} \begin{bmatrix} \bar{V}_1 & \bar{V}_2 & \bar{V}_3 \end{bmatrix}^T \tag{18}$$

where Δ is a real diagonal matrix with λ_1, λ_2 and λ_3, the eigenvalues of F, on its diagonal. Then, P is an orthogonal matrix with columns $\bar{V}_1, \bar{V}_2$ and $\bar{V}_3$ that represent the eigenvectors of F. These eigenvectors form an orthogonal basis and identify the principal directions of the quadric surface. Define a new vector $\bar{y} = [y_1 \quad y_2 \quad y_3]^T$ such that $\bar{y} = P^T \delta\bar{r}$. Equation (17) is then rewritten in the following canonical form

$$\bar{y}^T P^T F^T F P \bar{y} = \bar{y}^T \Delta^2 \bar{y} = \alpha_1 y_1^2 + \alpha_2 y_2^2 + \alpha_3 y_3^2 \leq \epsilon \tag{19}$$

where α_1, α_2 and α_3 correspond to λ_1^2, λ_2^2 and λ_3^2, respectively. Equation (19) represents an algebraic equation of degree two. In general, an equation of the second degree represents one of 17 different canonical forms that correspond to 17 canonical surfaces.[14] To determine the type of quadric surfaces derived from the canonical form in Equation (19), the following matrices are examined

$$e = \begin{bmatrix} \alpha_1 & 0 & 0 \\ 0 & \alpha_2 & 0 \\ 0 & 0 & \alpha_3 \end{bmatrix} \qquad E = \begin{bmatrix} \alpha_1 & 0 & 0 & 0 \\ 0 & \alpha_2 & 0 & 0 \\ 0 & 0 & \alpha_3 & 0 \\ 0 & 0 & 0 & -\epsilon \end{bmatrix} \tag{20}$$

The different types of quadric surfaces depend on the four following components:

- Λ = determinant of the E matrix
- ρ_e = rank of the e matrix
- ρ_E = rank of the E matrix
- $\alpha_1, \alpha_2, \alpha_3$ = characteristic roots of the e matrix

To identify a type of quadric surfaces from among the 17 forms, the following criteria are investigated: ρ_e, ρ_E, the sign of Λ and the signs of the characteristic roots of the e matrix. The characteristic roots, α_1, α_2 and α_3 defined in Equation (19) are all positive quantities and therefore they always have the same sign in this analysis. Table 2 summarizes the two types of quadric surfaces that are determined in this investigation by examining Equation (19). The real positive coefficient, ϵ, is small but never reaches zero precisely. Also, only the real domain is examined in this analysis. Therefore, the types of quadric surfaces to be investigated reduces to two: ellipsoids and elliptic cylinders. The specific type of quadric surfaces then depends on the

Table 2. Two types of quadric surfaces

Types of surface	ρ_e	ρ_E	Sign of Λ	Same sign for characteristic roots of e matrix
Ellipsoid	3	4	negative	yes
Elliptic cylinder	2	3	-	yes

given reference orbit and its corresponding eigenstructure. Consider the small halo reference orbit defined in Figure 1. At each location along this reference trajectory, the eigenvalues of the F matrix, λ_1, λ_2 and λ_3, are never equal or close to zero. Hence, the e and E matrices are full rank, i.e., $\rho_e = 3$ and $\rho_E = 4$, and only ellipsoids exist in the vicinity of this small halo orbit. These ellipsoids are illustrated in Figure 7(a).

One ellipsoid at time $t = 0$ days along the reference path appears in Figure 7(b). The size of the ellipsoids is enlarged for illustration in the figure. To derive these quadric surfaces, various distances between the chief spacecraft and the deputy vehicle are examined, from 0.1 km to 2 km, while maintaining a constant value for the ϵ coefficient. The eigenvectors of the F matrix, that is, $\bar{V}_1, \bar{V}_2$ and $\bar{V}_3$, corresponding to the respective eigenvalues are also plotted in Figures 7(a) and 7(b). They represent the three principal directions corresponding to the ellipsoids. The orientation of the ellipsoids in the $(\hat{x}, \hat{y})$-plane could also be related to

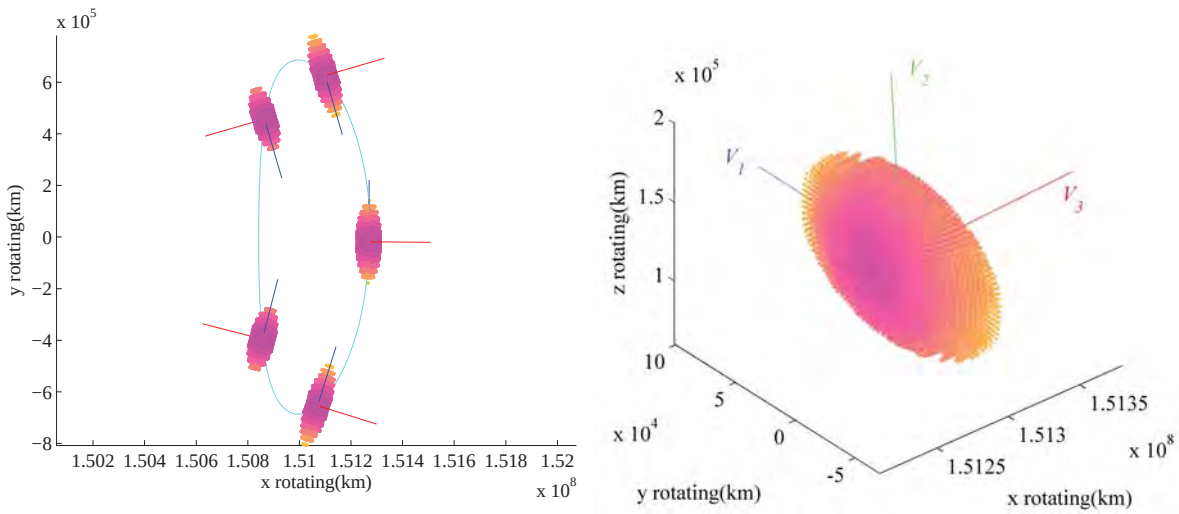

(a) (b)

Figure 7. (a) Ellipsoids along the small reference halo orbit (enlarged size for illustration); (b) One ellipsoid at time t = 0 days

the orientation of some regions suitable to maintain the mutual distances for a small formation of spacecraft. Gómez et al. derive small cones around a halo orbit with zero relative velocity and zero relative radial acceleration that ideally maintain the mutual distances between spacecraft.[8] By considering only the radial component of the relative acceleration, the small cones correspond to the following quadratic equation

$$\delta\bar{r}^T F \delta\bar{r} \leq \epsilon \tag{21}$$

which can be rewritten in its canonical form

$$\bar{y}^T P^T F P \bar{y} = \bar{y}^T \Delta \bar{y} = \lambda_1 y_1^2 + \lambda_2 y_2^2 + \lambda_3 y_3^2 \leq \epsilon \tag{22}$$

where $\bar{y}$, Δ and P are defined previously in Equations (19) and (20). To derive the cones, various small distances between the chief spacecraft and the deputy vehicle are examined, while varying the value for the ϵ coefficient with respect to the mutual distance between the spacecraft. The eigenvectors of the F matrix also represent the principal directions corresponding to the cones and, therefore, the cones derived by Gómez et al. possess the same orientation as the ellipsoids derived in this investigation given the same reference trajectory.

III.D. Quadric Surfaces along a Large Halo Orbit

A second halo reference with a significantly larger amplitude is now selected to investigate the effect of the reference path on the quadric surfaces. This large halo orbit is illustrated in Figure 1 and its A_y and A_z amplitudes are mentioned in Table 1. The quadric surfaces determined along this large reference orbit appear in Figure 8. The eigenvalues of the $F^T F$ matrix are examined along this new reference path. At some locations along the reference, the eigenvalue λ_1^2 approaches zero. Hence, at these positions on the reference, the e and E matrices defined in Equation (19) are singular with $\rho_e = 2$ and $\rho_E = 3$, and the quadric surfaces become elliptic cylinders at these particular locations (see Table 2). The two different types of quadric surfaces, i.e., ellipsoids and elliptic cylinders, are illustrated in Figures 9(a) and 9(b), respectively. The size of the quadric surfaces is enlarged in the figures for illustration. The close proximity of the Earth leads to a higher level of sensitivity in the vicinity of this large reference orbit. In particular, the left side

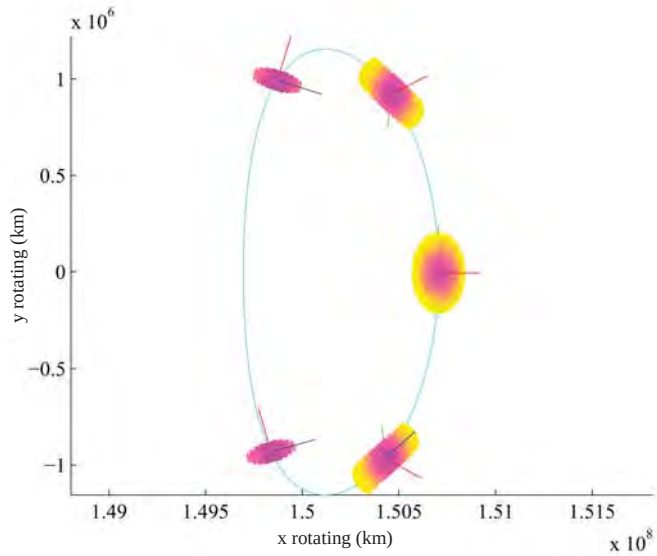

Figure 8. Ellipsoids and elliptic cylinders along the large reference halo orbit (enlarged size for illustration)

of this reference path represented in Figure 8 is in closest proximity with the Earth. As a consequence, no regions of zero drift are analytically indicated in the vicinity of this portion of the orbit.

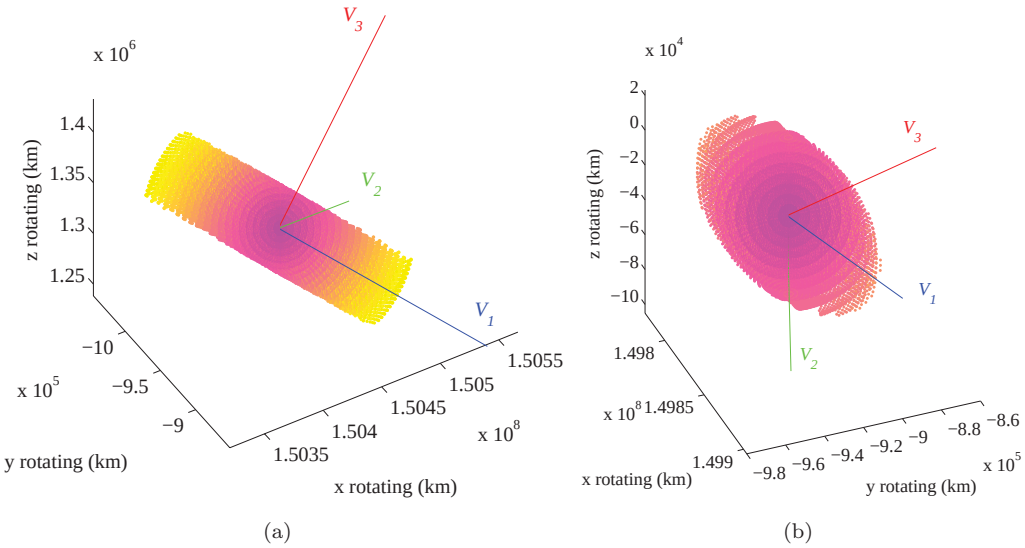

Figure 9. (a) One ellipsoid at time t = 36 days; (b) One elliptic cylinder at time t = 73 days (enlarged size for illustration)

IV. Natural Regions Suitable for Large Formations

The behavior at much larger distances from a specified reference trajectory due solely to the natural dynamics is explored for the placement of large formations of spacecraft. In this analysis, a two-spacecraft formation is investigated using a telescope as the chief spacecraft and an occulter as the deputy vehicle, one that is located at a relatively large distance from its telescope. The telescope evolves along one of the halo reference orbits defined in Figure 1. A fixed distance between the telescope and the occulter of 50,000 km is selected to develop the mission concept. Natural quasi-periodic Lissajous trajectories generated via multiple shooting algorithms are employed as a tool to examine relative motion in regions near the reference path. Such trajectories yield insight into the behavior of a large formation of spacecraft in this dynamical regime.

Directions for the large formation that yield small relative motion between the spacecraft are identified. Spheres of points at various locations along the reference orbit are developed that classify the orientation of a system at relatively large distances as orientations that yield small or large relative motions of the vehicles.

IV.A. Space Spheres

The natural flow at large distances from a given reference path is investigated by numerically generating trajectory arcs in the vicinity of the reference orbit. These trajectory arcs represent quasi-periodic Lissajous trajectories, that are computed using a multiple shooting scheme.[15] First, extensive computations of Lissajous trajectories near the telescope reference orbit are completed. The velocity vector along the telescope reference path and the corresponding Lissajous velocity vector are then investigated to determine regions that yield small or large relative motion between the spacecraft. At each instant of time, the velocity vector along the telescope orbit, denoted $\bar{V}_{ref}$, and the corresponding Lissajous velocity vector, denoted $\bar{V}_{liss}$, are compared as illustrated in Figure 10. In particular, the difference in the norm of the two velocities, as well

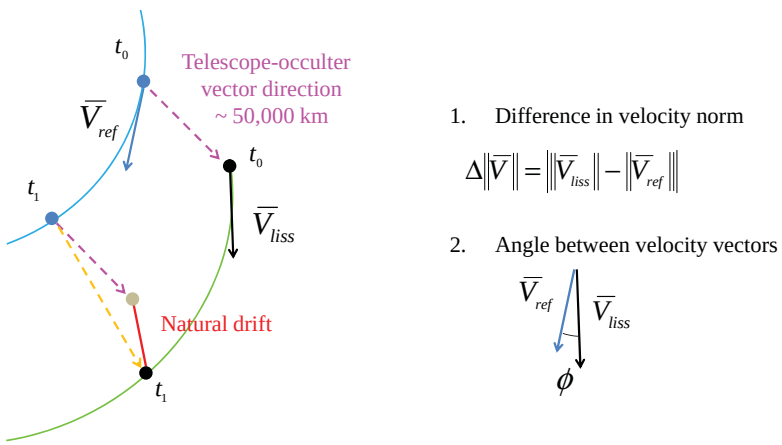

Figure 10. Schematic of the velocity vector comparison

as the angle between the two velocity vectors at each location around the telescope orbit, are derived. The natural drift of the telescope-occulter line-of-sight from its initial orientation depends on the size of these two parameters: difference in velocity norm and angle between velocity vectors. Figure 11 illustrates the variation of the telescope-occulter line-of-sight vector after a 3-day time interval with respect to these two parameters. At each location around the telescope orbit, a sphere of points with radius equal to the reference

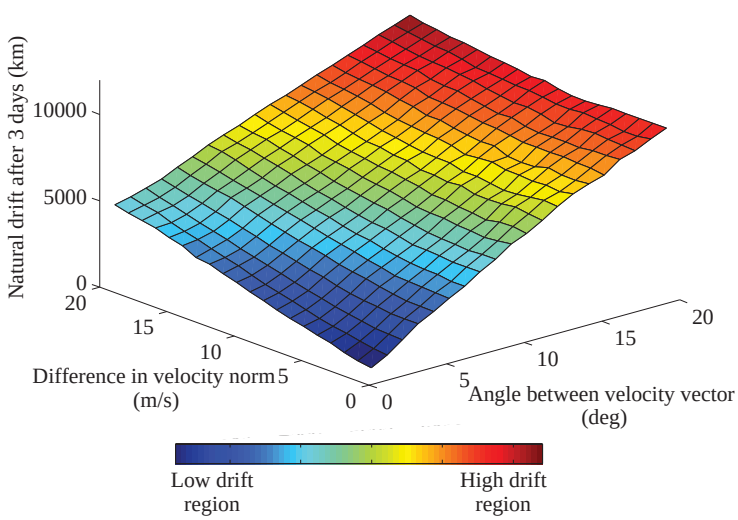

Figure 11. Variation of the telescope-occulter line-of-sight vector after a 3-day time interval with respect to the difference in the norm of the velocities and to the angle between the two velocity vectors

telescope-occulter distance is derived as illustrated in Figure 12(a). A vector originating at the center of the sphere (point on the reference orbit) and terminating at a point on the sphere defines a line-of-sight direction. On the surface of each sphere, different zones are defined that identify telescope-occulter directions (that is, line-of-sight orientations). Each point on the sphere is colored to reflect the value of the natural drift at that location. One space sphere at an isolated time appears in Figure 12(b). The blue zones represent regions

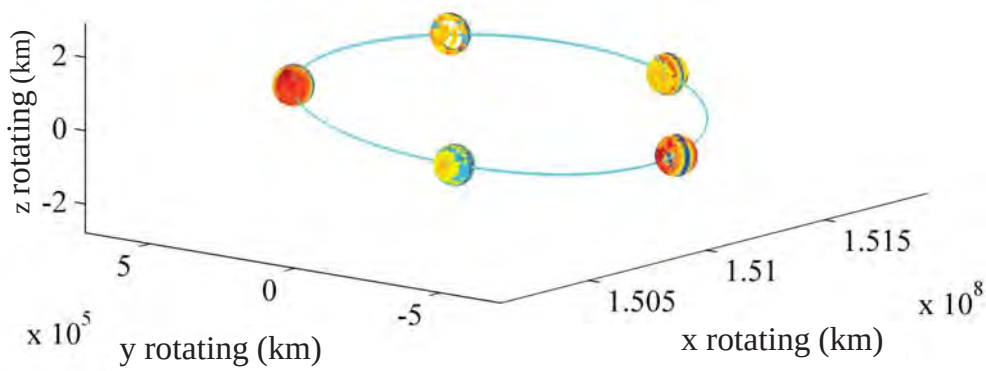

(a)

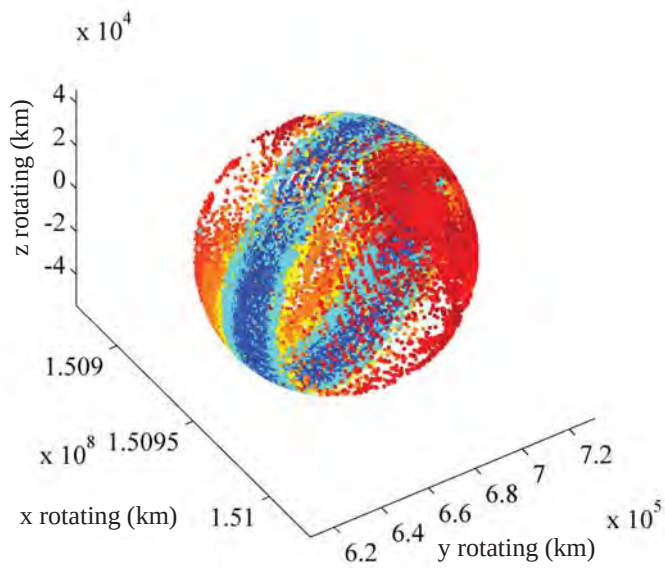

(b)

Figure 12. (a) Space spheres of 50,000 km radius at different times along the small halo reference orbit; (b) Space sphere at time t = 127 days along the small halo reference orbit

with less natural drift than the red zones. Effectively, if the line-of-sight to a star is directed along a line from the origin of the sphere to a blue dot, an occulter along this line experiences less natural drift than a star line-of-sight through a red dot. Locating the occulter in the regions with small natural drift leads to a smaller variation in the telescope-occulter vector, both in magnitude and pointing direction.

IV.B. Low Drift Regions on Space Spheres

The regions with low natural drift, derived on the space spheres, are now examined in detail. In particular, a correspondance with the quadric surfaces derived for small formations is established by examining the orientation of the low drift regions along the reference orbit. These regions represent ring-shaped objects, as illustrated in Figure 13(b). The three orthogonal vectors, $\bar{V}_1, \bar{V}_2$ and $\bar{V}_3$, represented in Figure 13(b), correspond to the eigenvectors of the $F^T F$ matrix derived from linear analysis. These eigenvectors represent the principal directions associated with the quadric surfaces derived via the variational equations. Given the projections of the low drift rings onto the $(\hat{x}, \hat{y})$-plane at different instants of time, the variations in the

orientation of the rings through time are observed. The low natural drift zones at different times along the telescope orbit appear in Figure 13(a). The dark blue rings reflect a difference in the velocity norm that is less than 5 m/s and an angle between the velocity vectors of less than 5 degrees, that correspond to the dark blue regions from the natural drift surface in Figure 11. In addition to the low natural drift zones, the three orthogonal eigenvectors of the $F^T F$ matrix are also illustrated in Figure 13 and appear in consistent colors across all the figures. Along the given small halo reference orbit, the low drift regions derived on the space sphere possess the same orientation as the quadric surfaces derived along the same reference path, as represented in Figure 4.

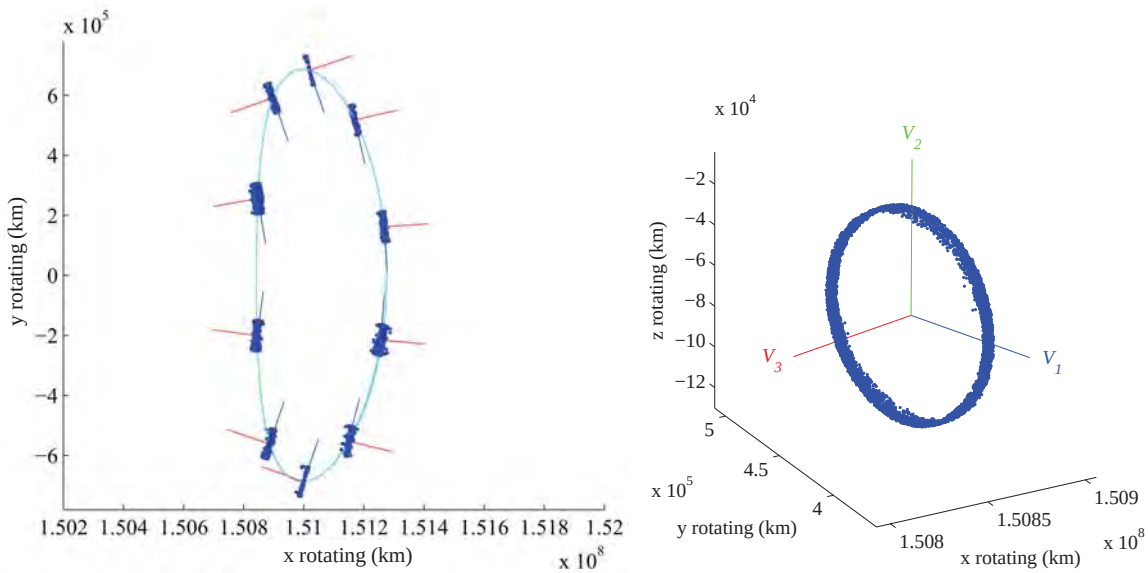

(a) (b)

Figure 13. (a) Low drift regions on the space spheres at different times along the small halo reference orbit; (b) One low drift region at time $t = 109$ days

It is interesting to compare the similarity of the quadric surfaces that describe the dynamics close to the reference orbit with the low drift regions at 50,000 km as illustrated in Figure 13. Both the low drift zones and the small quadric surfaces represent regions suitable to maintain a formation of spacecraft, either large or small. They are derived via significantly different methods, either from a linear analysis or numerically by propagating the state in the nonlinear dynamical model at a much larger relative distance. The surface of the small quadrics possesses no relative velocity and no relative acceleration whereas some relative velocity and relative acceleration still remain in the low drift regions (the difference in the velocity norm is less than 5 m/s and the angle between the velocity vectors is less than 5 degrees). But, interestingly, along this small halo reference orbit, they both are defined with the same orientation in space, as represented in Figure 13 and Figure 4, respectively.

IV.C. Low Drift Regions for Various Formation Sizes

The orientation of the low drift regions derived from the space spheres is investigated as the size of the large formation varies. Space spheres of various radii are computed along the given small halo reference orbit. The different radii selected are 12,500 km, 25,000 km, 50,000 km and 100,000 km, respectively. The low drift regions corresponding to these space spheres of various radii are then determined. The low drift regions that correspond to time $t = 109$ days along the reference path are illustrated in Figures 14(a) and 14(b). All the low drift zones of various radii reflect the same natural drift, that is, a drift that corresponds to a difference in the velocity norm that is less than 5 m/s and an angle between the velocity vectors of less than 5 degrees. As illustrated in Figure 14(b), the low drift regions all possess nearly the same orientation at any given times along the reference path and, this orientation, that correspond to the eigenspace of the linear system, seems to persist as the distance between the spacecraft increases to, at least, 100,000 km.

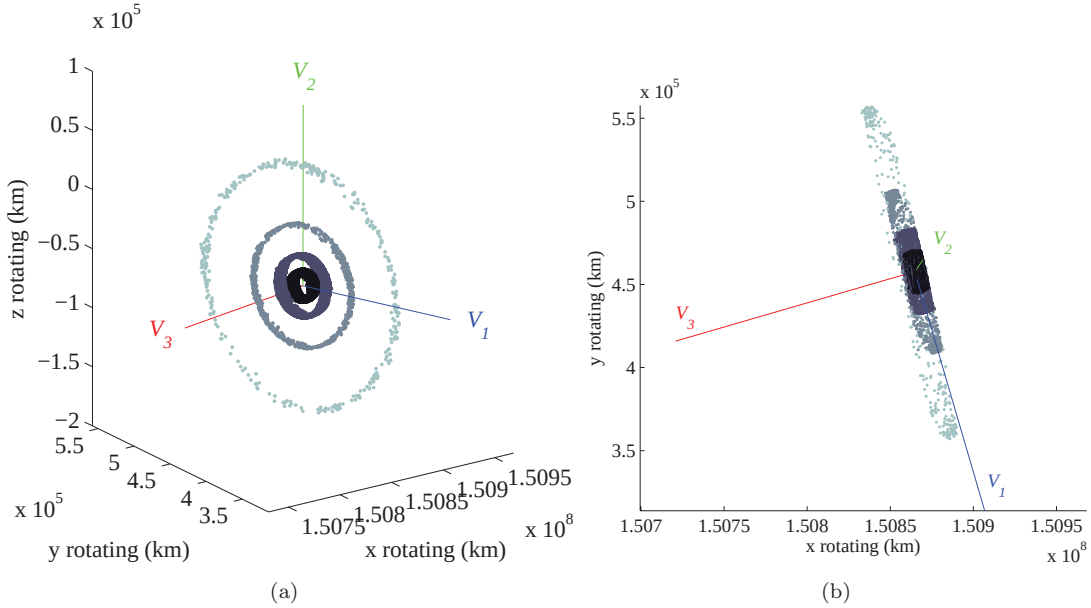

Figure 14. Low drift regions corresponding to various relative radii at time $t = 109$ days along the small halo reference orbit: (a) 3D view; (b) $(\hat{x}, \hat{y})$-projection

IV.D. Low Drift Regions Along a Large Halo Reference Orbit

The correspondance between the orientation of the low drift regions derived from the space spheres and the small quadric surfaces that are derived analytically is also investigated as the reference orbit varies. The large halo orbit, as defined in Figure 1, now represents the reference path for the telescope, and the computation of the space spheres is accomplished along this large halo reference path. Quasi-periodic Lissajous trajectories are computed in the vicinity of this new reference trajectory to determine the low drift regions at a distance of 50,000 km from the reference orbit. These low drift regions are illustrated in Figure 15. The regions of low relative drift reflect the same natural drift as the low drift regions derived at positions along the small halo reference orbit, i.e, they reflect a natural drift that corresponds to a difference in the velocity norm that is less than 5 m/s and an angle between the velocity vectors of less than 5 degrees. It is interesting to compare the orientation of the low drift regions to the three principal directions corresponding to the quadric surfaces, as derived along the same large halo reference orbit; these directions appear in Figure 8. At a given time along the reference path, in particular at locations where the quadric surfaces in Figure 8 are ellipsoids (i.e., when the F matrix of the linear system is full rank), the low drift regions at 50,000 km maintain a similar orientation in space as the ellipsoids. This scenario is illustrated at time $t = 73$ days in Figure 16(a). The principal directions of the low drift region at that time correspond quite closely to the eigenvector directions for the quadric surfaces, i.e., $\bar{V}_1$, $\bar{V}_2$ and $\bar{V}_3$, respectively. However, at a given time along the reference path, that correspond to a location where the F matrix becomes singular (one of its eigenvalues approaches zero), the low drift regions at 50,000 km are not correlated with the orientation of the quadric surfaces. This scenario is represented at time $t = 36$ days in Figure 16(b). The low drift region at that time is still represented by a ring of points but the orientation of the ring is not consistent with the eigenvector directions. At this time along the reference orbit, the quadric surfaces are represented by elliptic cylinders, as indicated in Figure 8. One eigenvalue of the F matrix, λ_1, approaches zero at this location. This singularity, derived from linear analysis, allows for more than one possible orientations for the low drift regions. These new orientations are only determined using the nonlinear system and are not derived directly via the variational equations.

V. Star Observations using the Space Spheres

The effectiveness of the low natural drift regions derived for large formations is evaluated for the observation of inertially-fixed target stars at different times along the telescope orbit. Although inertially-fixed

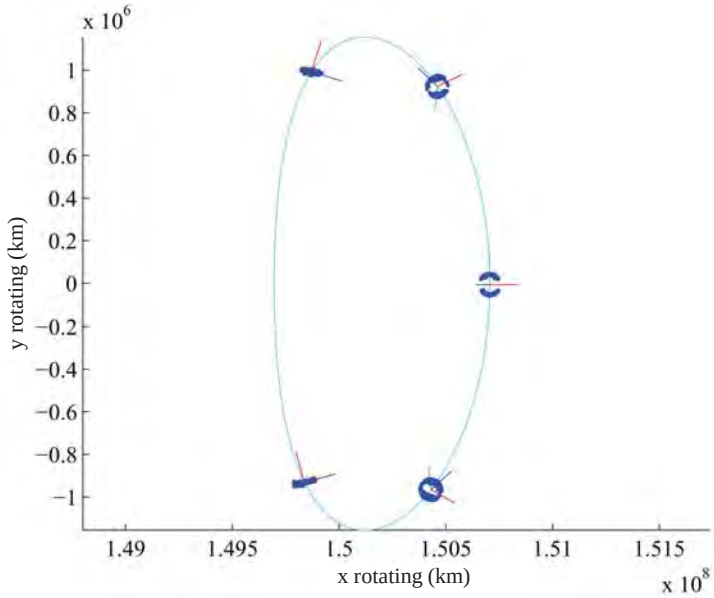

Figure 15. Low drift regions for a distance of 50,000 km between the telescope and occulter, at various locations along the large halo reference orbit

target stars describe paths that are not fixed in the rotating frame, the natural motion of a fixed star relative to the rotating frame is still smaller than the natural drift at a relative position within 50,000 km which defines the low drift regions.

V.A. Locations along the Telescope Orbit for Star Observations

The direction of an inertial target star is usually specified in terms of two angles, the right ascension and the declination, defined in the equatorial frame. The direction is time dependent as viewed from the rotating frame of the CR3BP and, therefore, a coordinate transformation is necessary to locate the star, i.e., the target direction, at each instant of time. The coordinate transformation from the equatorial frame to the rotating frame is derived as

$$\begin{bmatrix} x \\ y \\ z \end{bmatrix}_{Rotating} = \begin{bmatrix} \cos\delta & \cos\zeta\sin\delta & \sin\zeta\sin\delta \\ -\sin\delta & \cos\zeta\cos\delta & \sin\zeta\cos\delta \\ 0 & -\sin\zeta & \cos\zeta \end{bmatrix} \begin{bmatrix} x \\ y \\ z \end{bmatrix}_{Equatorial} \tag{23}$$

where $\zeta = 23.0075$ degrees, $\delta = \omega t + \delta_0$, and δ_0 represents the initial angle between the inertial and rotating frames (δ_0 is assumed to be equal to zero in this analysis); the angular rate ω is equal to one in nondimensional coordinates. The vector direction of the target star in terms of the rotating frame is rewritten in spherical coordinates as

$$\begin{bmatrix} x \\ y \\ z \end{bmatrix}_{Rotating} = \begin{bmatrix} \cos\lambda\cos\gamma \\ \cos\lambda\sin\gamma \\ \sin\lambda \end{bmatrix} \tag{24}$$

The in-plane angle γ, measured relative to the $\hat{x}$-axis in the rotating frame, and the out-of-plane angle λ, measured relative to the $(\hat{x}, \hat{y})$ rotating plane, are illustrated in Figure 17(a). The out-of-plane angle λ corresponding to a given inertially-fixed target star remains constant with time in the rotating frame. However, the in-plane angle γ varies with time in the $(\hat{x}, \hat{y})$ rotating plane, approximatively 1 degree/day, and therefore, the direction to the target star might eventually lie in a low drift zone at a specific time along the telescope orbit.

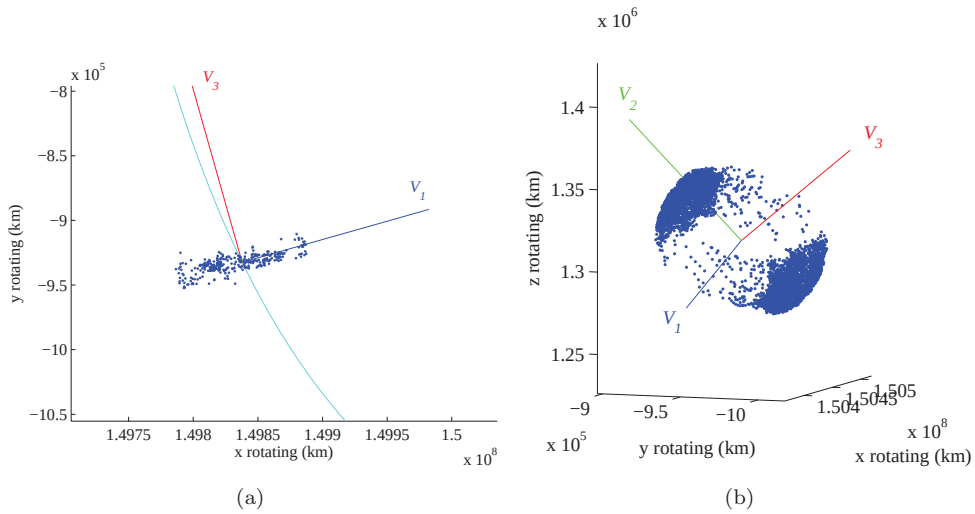

(a) (b)

Figure 16. Low drift regions along the large halo reference orbit: (a) At time $t = 73$ days ; (b) At time $t = 36$ days

V.B. Orientation of the Low Drift Regions

The low drift regions over each space sphere are represented now by two orientation angles. These ring-shaped regions are defined by an in-plane angle θ, measured relative to the $\hat{x}$-axis in the rotating frame, and an out-of-plane angle β, oriented with respect to the $(\hat{x}, \hat{y})$ rotating plane. These angles appear in Figure 17(b). Some characteristics of these low drift regions are apparent by examining the in-plane angle θ along one

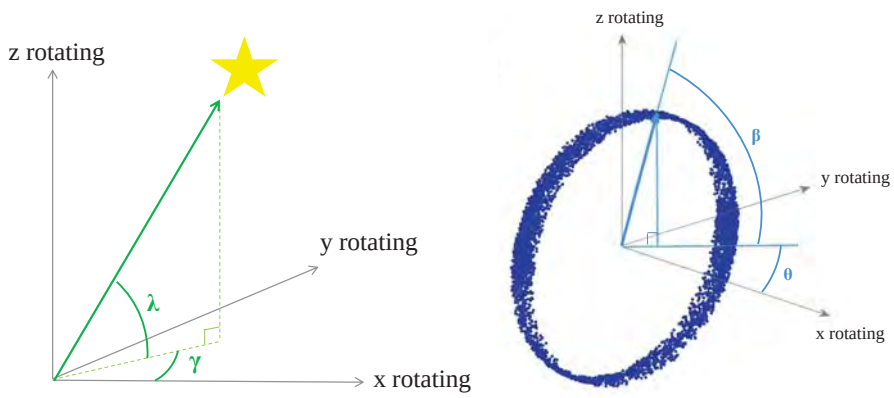

(a) (b)

Figure 17. (a) Star direction described by in-plane angle γ and out-of-plane angle λ in the rotating frame; (b) Low drift region on a space sphere described by in-plane angle θ and out-of-plane angle β

revolution of the orbit as illustrated in Figure 13. The low drift directions identified by blue points feature an in-plane angle θ that approaches either 90 or -90 degrees at each time along one revolution of the orbit. The mean value of the angle θ over all the blue dots in the entire ring is calculated at each time along the telescope orbit.This mean value is then compared to the in-plane angle γ corresponding to the inertial target star direction. The low drift regions are three-dimensional ring-shaped objects, and therefore, matching the in-plane angles also assures that the out-of-plane angle of the star corresponds to an out-of-plane angle in the blue regions. The closest value between the in-plane angle of the star and the mean value of the angle θ occurs at the seemingly "best" location along the telescope orbit, and this location ensures that the star direction lies in a low natural drift region during the observation phase. The skematic in Figure 18 illustrates this process. Two space spheres are represented at time t_1 and time t_2. The low drift regions and the high drift regions are represented in blue and red, respectively, over each sphere. Given an inertial star direction for observation (Star 1 in the skematic), if the observation is initiated at time t_1, the occulter lies in a high

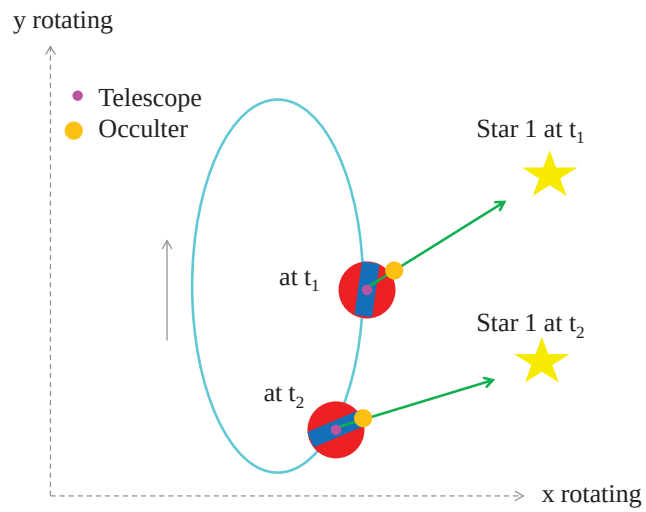

Figure 18. Skematic to assess the starting times for observation

drift zone and the control to maintain it along the line-of-sight is relatively high. However, if the observation of the same star is delayed to begin at time t_2, the occulter lies in a low drift region at this time, and therefore the cost of the control may be reduced. An example for one inertial target star appears in Figure 19. The

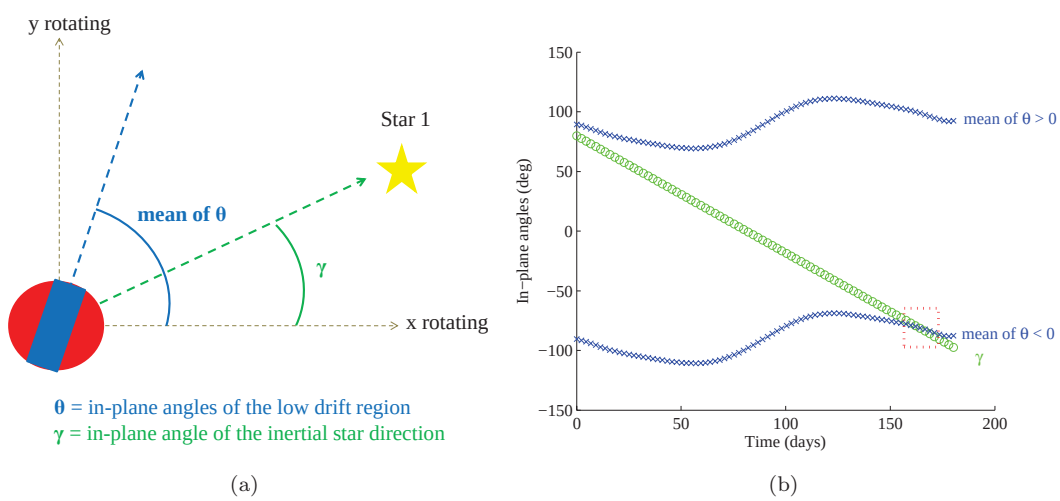

Figure 19. Best locations along the telescope orbit to begin observation: Example with one inertial star direction. The "best" location to initiate the observation is approximately 160 days (red square)

star direction is indicated by a right ascension of 80 degrees and a declination of 10 degrees. The in-plane angle, γ, corresponding to the inertial target star is represented in green in Figure 19(b) as computed at each time along the telescope orbit. As noted in the figure, γ shifts approximately 1 degree/day. The best location to initiate the observation of this specific target star is near the time $t = 160$ days, that is, the time at which the value of γ is close to the mean value of the angle θ as indicated in the figure by the dotted red square.

V.C. Control Strategy for Star Observations

Even in the low drift regions, drift between the two spacecraft (telescope and occulter) still occurs and the design of a controller to maintain the formation is necessary. An LQR controller is selected to maintain the occulter along the line-of-sight from the telescope to the inertial target stars. If the specific orientation of the formation lies in a zone of low natural drift, then the control to maintain the orientation is reduced. The telescope is assumed to move along the small halo reference orbit represented in Figure 1. Given an

inertial target star direction with an observation time of 20 days, the occulter must be maintained precisely along the line-of-sight from the telescope to the star over the entire observation interval. In particular, the occulter is constrained to remain within ±100 km of the baseline path in the radial direction (line-of-sight direction) and within a few meters from the baseline position in the transverse direction (orthogonal to the line-of-sight).[16,17] Various reference arcs are computed for different starting locations along the telescope orbit. These reference arcs are selected as potential baseline paths for the occulter along the telescope line-of-sight to the inertially fixed star. An LQR controller is formulated to track these reference arcs during the observation period. The motion of the occulter in the CR3BP is described in terms of the following differential equations

$$\ddot{x} = f_x(x, \dot{x}, y, \dot{y}, z, \dot{z}) + u_x \tag{25}$$

$$\ddot{y} = f_y(x, \dot{x}, y, \dot{y}, z, \dot{z}) + u_y \tag{26}$$

$$\ddot{z} = f_z(x, \dot{x}, y, \dot{y}, z, \dot{z}) + u_z \tag{27}$$

wheref_x, f_y, f_z are defined from Equation (3)-Equation (5) as

$$f_x = U_x + 2\dot{y} \tag{28}$$

$$f_y = U_y - 2\dot{x} \tag{29}$$

$$f_z = U_z \tag{30}$$

and $\bar{u} = [u_x \quad u_y \quad u_z]^T$ is the control vector. Let $\bar{X}_0$ be some reference arc and $\bar{u}_0$ the associated control effort to maintain $\bar{X}_0$. The selected reference arcs represent the baseline paths of the inertial star directions in the rotating frame. During a star observation, the locations of the inertially-fixed target star in the rotating frame are computed at the distance of 50,000 km from the telescope over the observation interval. These locations correspond to the star reference path as illustrated in Figure 20. The occulter is controlled

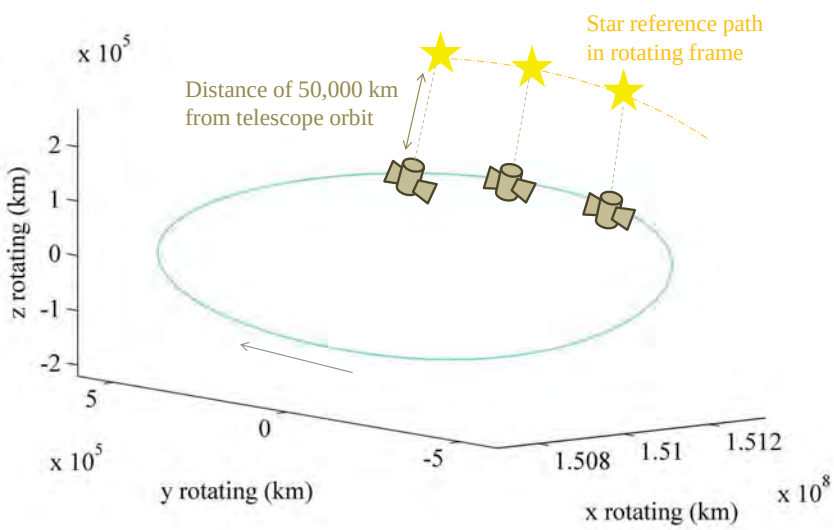

Figure 20. Baseline reference path of inertial star direction computed at 50,000 km from the telescope in the rotating frame

to track these reference arcs using the LQR controller. Linearization relative to these reference solutions yields a linear system of the form

$$\delta\dot{\bar{X}} = A(t)\delta\bar{X} + B(t)\delta\bar{u} \tag{31}$$

where $\delta\bar{X}$ and $\delta\bar{u}$ are the variations relative to the reference arc $\bar{X}_0$ and its respective reference control $\bar{u}_0$. The time-varying matrix $A(t)$ is the matrix corresponding to the variational equations defined in Equation (7) and evaluated along the star reference arc and $B(t) = [0_{3,3} \quad I_{3,3}]^T$.

The observation of the given target star is computed at three different starting times around the telescope orbit. The telescope in its reference orbit appears in cyan in Figure 21. Then, the path of the occulter controlled via the LQR controller is plotted in blue for the three different starting times. For a given starting time, the LQR controller tracks the reference path, which corresponds to the path of the inertial target star

in the rotating frame at 50,000 km from the telescope orbit. With knowledge of the low drift zones, the best correlation between locations along the telescope orbit and the occulter drift is identified to ensure that the star direction lies in a low natural drift region. The strategic time of observation for this particular star was determined as time $t = 7$ days using the low drift regions. For comparison, two other starting times, $t = 80$ days and $t = 120$ days are also plotted in Figure 21. The direction to the star at each of these starting times is represented by a red star. The observation phase lasts for 20 days in this example. The total cost associated with each of these observations is illustrated in Figure 22. The cost of observation is reduced if the observation begins near the time $t = 7$ days, that is, the time that corresponds to the low drift direction. Therefore, observing the stars at the strategic times via the low drift zones reduces the control effort during the observation phase, particularly for longer observation intervals.

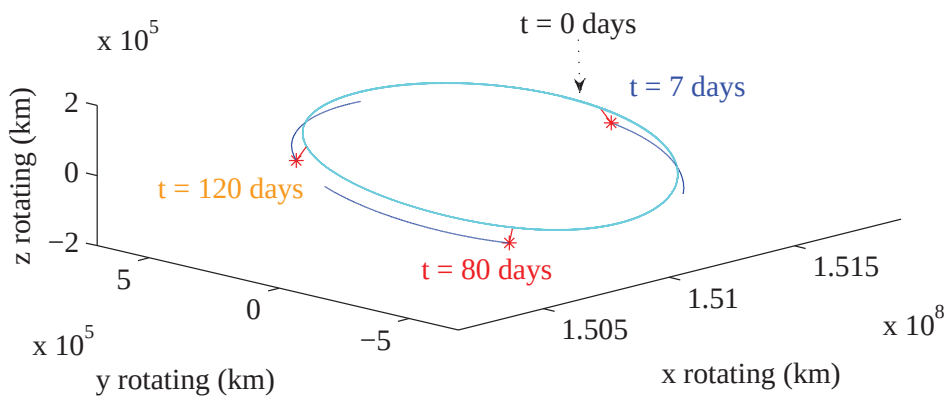

Figure 21. Path of the occulter for the observation of the same target star originating at different locations around the telescope orbit

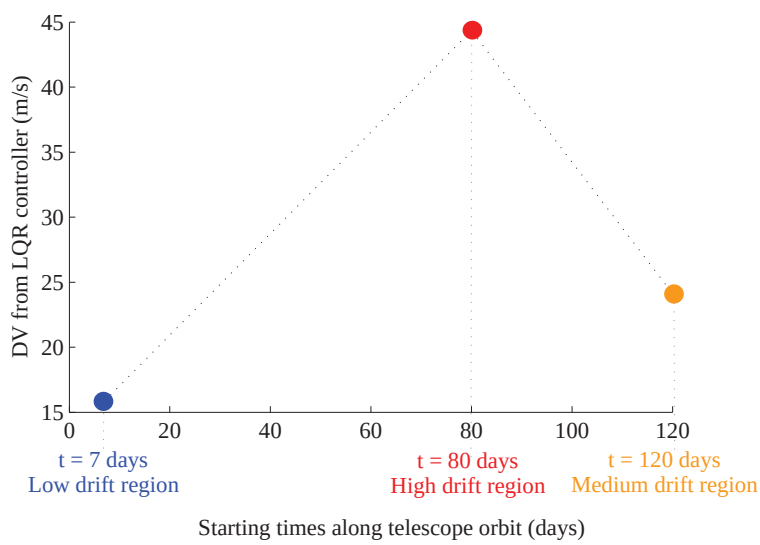

Figure 22. Cost associated with the observation of the selected target star at the different starting times

VI. Summary and Concluding Remarks

In this present investigation, the natural dynamics in the L_2 Sun-Earth libration point region are exploited to aid in the control of a formation of spacecraft. Natural zones that exhibit low relative drift are derived such that large variations in the mutual distances between the spacecraft are prevented while maintaining the orientation of the formation. For small formations, these low drift regions represent quadric surfaces and they are derived analytically using variational equations with respect to the reference trajectory. For much larger formations, the low drift zones are examined numerically by propagating in the nonlinear dynamical

model at a much larger relative distance from the reference path. The effectiveness of these low drift regions is then demonstrated to reduce the control effort to maintain a large telescope-occulter formation during the observation of inertially-fixed target stars.

Although this work is motivated by the telescope-occulter mission design, it also offers some insight into the relative motion between vehicles separated by either small or large distances and this knowledge is useful for various applications. Further exploration of the natural dynamics in the Sun-Earth system or other systems may be examined for the placement of small or large formations.This current analysis focuses essentially on the L_2 Sun-Earth libration point region. The northern halo family provides the reference trajectories needed in this investigation but other reference trajectories may be exploited for formation flying as well. New reference trajectories may include other periodic orbits, such as vertical, axial or resonant orbits, as well as unstable and stable manifold arcs for transfer trajectories of multiple spacecraft. By investigating different environments or various reference trajectories, some potential new characteristics for the low drift regions may be determined.

VII. Acknowledgment

The authors wish to thank Purdue University and the School of Aeronautics and Astronautics for providing financial support. The computational capabilities available in the Rune and Barbara Eliasen Aerospace Visualization Laboratory are also appreciated.

References

[1]W. Cash and the New Worlds Team, "The New Worlds Observer: the Astrophysics Strategic Mission Concept Study," *EPJ Web of Conferences*, Vol. 16, July 2011. DOI 10.1051/epjconf/20111607004.

[2]B. T. Barden and K. C. Howell, "Fundamental Motions Near Collinear Libration Points and Their Transitions," *Journal of the Astronautical Sciences*, Vol. 46, October-December 1998, pp. 361–378.

[3]K. C. Howell and B. G. Marchand, "Natural and Non-Natural Spacecraft Formations Near the L1 and L2 Libration Points in the Sun-Earth/Moon Ephemeris System," *Dynamical Systems: an International Journal, Special Issue: Dynamical Systems in Dynamical Astronomy and Space Mission Design*, Vol. 20, March 2005, pp. 149–173.

[4]G. Gómez, M. Lo, J. Masdemont, and K. Museth, "Simulation of Formation Flight Near L2 for the TPF Mission," *AAS Astrodynamics Specialist Conference*, Quebec City, Canada, August 2001. Paper No. AAS 01-305.

[5]B. G. Marchand and K. C. Howell, "Control Strategies for Formation Flight in the Vicinity of the Libration Points," *Journal of Guidance, Control, and Dynamics*, Vol. 28, November-December 2005, pp. 1210–1219.

[6]F. Y. Hsiao and D. J. Scheeres, "Stabilizing Motion Relative to an Unstable Orbit: Applications to Spacecraft Formation Flight," *Journal of Guidance, Control, and Dynamics*, Vol. 26, January-February 2003.

[7]F. Y. Hsiao and D. J. Scheeres, "Design of Spacecraft Formation Orbits Relative to a Stabilized Trajectory," *Journal of Guidance, Control, and Dynamics*, Vol. 28, July-August 2005.

[8]G. Gómez, M. Marcote, J. Masdemont, and J. Mondelo, "Zero Relative Radial Acceleration Cones and Controlled Motions Suitable for Formation Flying," *Journal of the Astronautical Sciences*, Vol. 53, No. 4, 2005, pp. 413–431.

[9]M. Lo, "External Occulter Trajectory Study," *NASA JPL*, September 2006.

[10]L. Millard and K. C. Howell, "Optimal Reconfiguration Maneuvers for Spacecraft Imaging Arrays in Multi-Body Regimes," *Acta Astronautica*, Vol. 63, December 2008, pp. 1283–1298. DOI: 10.1016/j.actaastro.2008.05.

[11]E. Kolemen and J. Kasdin, "Optimal Trajectory Control of an Occulter-Based Planet-Finding Telescope," *Advanced in Astronautical Science*, Vol. 128, 2007, pp. 215–233. Paper No. AAS 07-037.

[12]A. Héritier and K. C. Howell, "Natural Regions Near the Sun-Earth Libration Points Suitable for Space Observations with Large Formations," *AAS/AIAA Astrodynamics Specialist Conference*, Girdwood, Alaska, August 2011. Paper No. AAS 11-493.

[13]L. P. Virgili, "Design and Evaluation of Navigation and Control Algorithms for Spacecraft Formation Flying Missions," *Ph.D. Thesis*, Universitat de Barcelona, Barcelona, Spain, 2006.

[14]D. Hilbert and S. Cohn-Vossen, "The Second-Order Surfaces," *Geometry and Imagination*, Vol. 3, 1999, pp. 12–19.

[15]A. Héritier, "Exploration of the Region near the Sun-Earth Collinear Libration Points for the Control of Large Formations," *Ph.D. Thesis*, Purdue University, West Lafayette, Indiana, 2012.

[16]L. Millard and K. C. Howell, "Control of Spacecraft Occulter Arrays in Multi-Body Regimes," *AAS/AIAA Astrodynamics Specialists Conference*, Honolulu, Hawaii, August 2008.

[17]R. Luquette and R. Sanner, "Spacecraft Formation Control: Managing Line-of-Sight Drift Based on the Dynamics of Relative Motion," *3rd Int. Symp. Formation Flying, Missions, and Technologies*, Noordwijk, The Netherlands, April 2008.